Available online at www.sciencedirect.com

ScienceDirect

Ceramics International 40 (2014) 3105–3116

CERAMICS INTERNATIONAL

www.elsevier.com/locate/ceramint

Preparation and characterization of basic carbonates as novel anode materials for lithium-ion batteries

Lianyi Shao, Kaiqiang Wu, Xinxin Jiang, Miao Shui, Rui Ma, Mengmeng Lao, Xiaoting Lin, Dongjie Wang, Nengbing Long, Jie Shu*

Faculty of Materials Science and Chemical Engineering, Ningbo University, Ningbo 315211, Zhejiang Province, People's Republic of China

Received 16 September 2013; received in revised form 29 September 2013; accepted 30 September 2013
Available online 7 October 2013

Abstract

Three basic carnobates, $(PbCO_3)_2 \cdot Pb(OH)_2$, $NiCO_3 \cdot 2Ni(OH)_2 \cdot 4H_2O$, and $CuCO_3 \cdot Cu(OH)_2$, are prepared and used for the first time as anode materials for lithium-ion batteries. Electrochemical results show that $(PbCO_3)_2 \cdot Pb(OH)_2$, $NiCO_3 \cdot 2Ni(OH)_2 \cdot 4H_2O$ and $CuCO_3 \cdot Cu(OH)_2$ can deliver high initial discharge capacities of 1175.8, 1742.6 and 1356.2 mAh g^{-1}, respectively. The lithium storage mechanisms of basic metal carbonates are observed by various electrochemical, *ex-situ* and *in-situ* methods during the initial charge–discharge cycle. It can be found that basic metal carbonates decompose into metal (M = Pb, Ni or Cu), Li_2CO_3, LiOH and H_2O upon the preliminary discharge. With further lithiation, the active metal can alloy with Li to form several Li_xM phases. During the reverse charge process, Li extraction from the de-alloying reaction, M/Li_2CO_3 and M/LiOH mixtures can be observed. However, the cycling efficiency is low. Electrochemically inactive particles generated from pulverization, structural collapse and electronic contact loss result in the large irreversible capacity and low initial cycling efficiency. By using carbon black as conductive additive and buffer layer, the electrochemical properties of composite can be greatly improved. Carbon black–$(PbCO_3)_2 \cdot Pb(OH)_2$ composite shows a reversible charge capacity of 244.7 mAh g^{-1} after 20 cycles, which is much higher than the value (77.2 mAh g^{-1}) of the pristine sample.

Keywords: A. Powders: chemical preparation; B. X-ray methods; C. Electrical properties; E. Batteries

1. Introduction

Lithium-ion batteries, as the potential attractive green energy sources for hybrid/electric vehicles and consumer electronics, have attracted significant interests in the past 3 decades owing to their high capacity, superior stability and environmentally friendly characteristics. As the anode material in lithium-ion batteries, carbon-based materials such as artificial graphite are usually used as the standard electrodes in the present day due to their good electronic conductivity and low volume change during the lithiation and delithiation process [1]. Nevertheless, their poor rate performance (low Li ion diffusion coefficient), serious safety issue (low Li ion insertion potential), and their low capacity (theoretical capacity of graphite is 372 mAh g^{-1}) cannot make the carbon-based anode materials match the demand of the progressive modern industry [2,3]. Consequently, many substitution materials have been exploited.

Recently, transition metal oxides (M_xO_y, where M is Cu, Ni, Co, Mn, or Fe) have shown great potential as anode materials for lithium-ion batteries owing to their high safety, high theoretical capacity, low cost and environmental friendliness [4–11]. Unfortunately, there are still many challenging issues in using them for lithium-ion batteries. One obstacle is their power performance, resulting from their low intrinsic electronic conductivity. Another hindrance is the poor cycle performance due to the severe volume expansion during cycling process and the formation of unstable solid electrolyte interphase (SEI) film [7,12].

In the most recent years, several metal carbonates, such as manganese carbonate [13], cobalt carbonate [14,15], $Mn_{1-x}Co_xCO_3$ [16], $(BiO)_2CO_3$ and $CdCO_3$ [17], have been considered as potential candidates for anode materials in lithium-ion batteries due to high reversible capacity, good

*Corresponding author. Tel.: +86 574 87600787; fax: +86 574 87609987.
E-mail addresses: sergio_shu@hotmail.com, shujie@nbu.edu.cn (J. Shu).

0272-8842/$ - see front matter © 2013 Elsevier Ltd and Techna Group S.r.l. All rights reserved.
http://dx.doi.org/10.1016/j.ceramint.2013.09.136

capacity retention and excellent cycle calendar life. Nevertheless, no literatures about basic carbonates as anode materials for lithium-ion batteries were ever reported. In this paper, we firstly report the electrochemical performance of basic metal carbonates as anode materials by using cyclic voltammetry and galvanostatic charge–discharge techniques. Moreover, further studies are undertaken to clarify the electrochemical reaction mechanisms of basic metal carbonates with Li by various *ex-situ* and *in-situ* techniques.

2. Experimental

In this work, $NiCO_3 \cdot 2Ni(OH)_2 \cdot 4H_2O$, $(PbCO_3)_2 \cdot Pb(OH)_2$ and $CuCO_3 \cdot Cu(OH)_2$ were prepared by a co-precipitation method using $NiSO_4 \cdot 6H_2O$, $Pb(NO_3)_2$, $CuSO_4 \cdot 5H_2O$ as raw materials and $Na_2CO_3 \cdot 10H_2O$ as precipitant. All the chemical reagents were analytical grade and obtained from Sinopharm Chemical Reagent Co. Ltd. in China. The obtained deposits were dried at 80 °C under vacuum before use.

2.1. Samples characterization

The crystallographic structure of the samples was determined by the X-ray diffraction (XRD, Bruker AXS D8 Focus diffractometer) using Cu Kα ($\lambda = 0.15406$ nm) radiation. The surface morphology and microstructure of the samples were characterized by scanning electron microscopy (SEM, JEOL S3400). Selected area electron diffraction (SAED) and high resolution transmission electron microscopy (HRTEM) measurements were performed on JEOL JEM-2100. Thermogravimetric (TG) and differential thermal analysis (DTA) curves were obtained in a Seiko TG/DTA 7300 instrument under argon atmosphere.

To investigate the reaction mechanisms in the basic carbonates, *ex-situ* XRD and *ex-situ* Fourier transform infrared spectroscopy (FTIR, Nicolet FTIR-6700) patterns of basic carbonates were collected at selected capacities during the initial discharge and charge process. The lithiated and delitiated samples for *ex-situ* XRD were prepared in an argon-filled glove box, dried under vacuum condition, and put in the sample holder covering with a polymer film, then immediately analyzed by XRD in the angle range from 10° to 80°. The lithiated and delitiated samples for *ex-situ* FTIR were washed by dimethyl carbonate and vacuumed for 5 h before mixing with KBr. The semi-transparent slices were pressed and prepared using the mixed powder in the argon-filled glove box and transferred to the sample chamber within 10 s. The semi-transparent slices were studied by Nicolet FTIR-6700 instrument under argon environment.

2.2. Electrochemical characterization

The working electrodes were prepared by blending the basic carbonates, carbon black (CB) and polyvinylidene fluoride at the weight ratio of 4:1:1 in N-methylpyrodine and pasted on a Cu foil. The working electrodes were dried at 120 °C under vacuum condition for 12 h and then cut into discs with a diameter of 15 mm. In the simulated batteries, a pure lithium metal foil (Jiangxi Ganfeng Lithium Co. Ltd.) was used as counter electrode. The organic electrolyte (Zhangjiagang Guotai Huarong New Chemical Materials Co. Ltd.) was

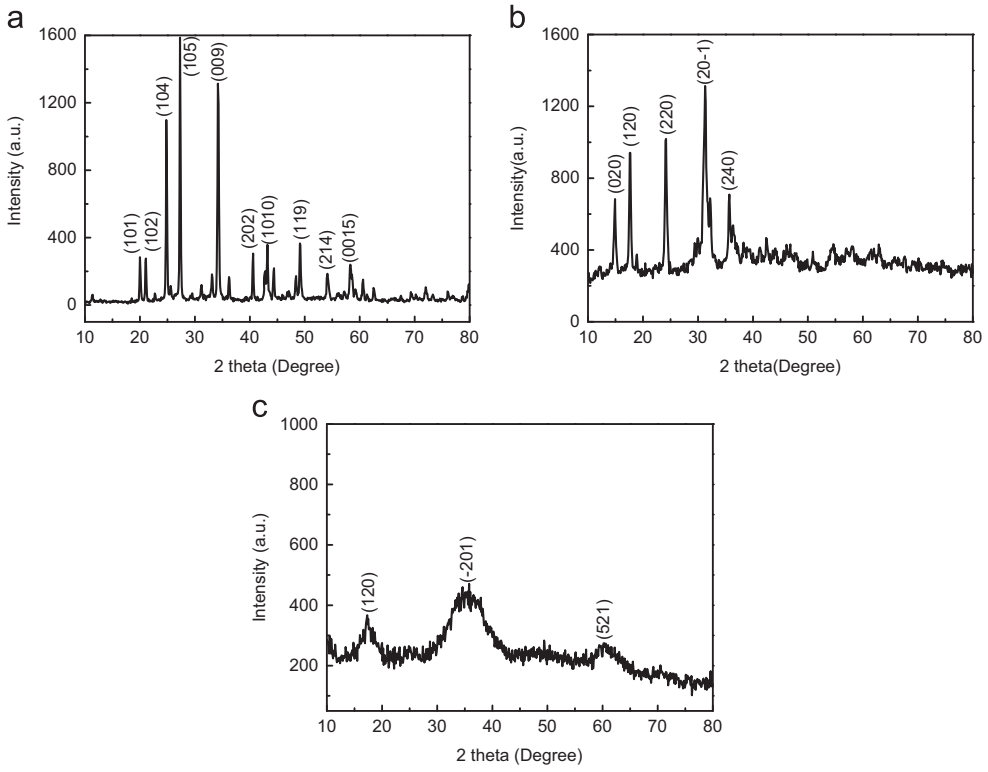

Fig. 1. XRD patterns of (a) $(PbCO_3)_2 \cdot Pb(OH)_2$, (b) $CuCO_3 \cdot Cu(OH)_2$ and (c) $NiCO_3 \cdot 2Ni(OH)_2 \cdot 4H_2O$.

composed of 1 mol L^{-1} solution of $LiPF_6$ in a mixture of dimethyl carbonate and ethylene carbonate (DMC:EC = 1:1, v/v). Besides, Whatman glass fiber was used as separator. The simulated batteries were assembled in the argon-filled glove box.

Galvanostatic charge–discharge experiments for simulated batteries were performed at a constant current density of 50 mA g^{-1} in the potential range of 0.0–3.0 V by using multichannel Land battery test system instrument (Wuhan Jinnuo, China). The electrochemical impedance spectra were performed on a CHI 660D electrochemical workstation (Shanghai Chenhua, China) at room temperature. Cyclic voltammetry (CV) tests were carried out at a scanning rate of 0.1 mV s^{-1} between 0.0 and 3.0 V on EC-Lab electrochemical workstation (Bio-Logic VSP3, France).

3. Results and discussion

The typical XRD patterns of $(PbCO_3)_2 \cdot Pb(OH)_2$, $CuCO_3 \cdot Cu(OH)_2$ and $NiCO_3 \cdot 2Ni(OH)_2 \cdot 4H_2O$ are shown in Fig. 1. The characteristic diffraction peaks at 24.7°, 27.3°, and 34.1° can be indexed to the (104), (105) and (009) planes of hexagonal $(PbCO_3)_2 \cdot Pb(OH)_2$ (JCPDS card no. 10-0401). The main diffraction peaks at 17.6°, 24.1° and 31.2° can be assigned to the (120), (220) and (20−1) reflections of monoclinic $CuCO_3 \cdot Cu(OH)_2$ (JCPDS card no. 41-1390). The broad humps at 17.6°, 34.8° and 60.6° can be attributed to the (120), (−2 0 1) and (521) reflections of monoclinic $NiCO_3 \cdot 2Ni(OH)_2 \cdot 4H_2O$ (JCPDS card no. 35-0501) respectively. The broad diffraction peaks suggest that the crystalline size of the $NiCO_3 \cdot 2Ni(OH)_2 \cdot 4H_2O$ sample is small.

Fig. 2a–c exhibits the SEM images of the three basic carbonates. It is obvious that the hexagonal $(PbCO_3)_2 \cdot Pb(OH)_2$ (Fig. 2a) is mainly composed of granules and slabs with the particle size of 200–800 nm. As shown in Fig. 2b, the $CuCO_3 \cdot Cu(OH)_2$ particles exhibit imperfect round shape and the diameter is about 100–200 nm. For $NiCO_3 \cdot 2Ni(OH)_2 \cdot 4H_2O$ (Fig. 2c), lots of nanoparticles with the particle size of about 20–40 nm agglomerate together to form larger secondary particles.

The TG-DTA curves for basic carbonates under argon atmosphere are shown in Fig. 3. As shown in Fig. 3a, two endothermic peaks at 246.1 and 334.1 °C are observed, corresponding to three weight loss stages. The initial stage occurs between 142.2 and 224.7 °C attributed to the formation of $(PbCO_3)_2 \cdot PbO$ and water. This stage gives a weight loss of 1.5% at 224.7 °C in accordance with the expected value (2.3%) for the Eq. (1). The second stage begins immediately after the initial stage and ends at 255.4 °C with a weight loss of 5.0% in good agreement with the expected value (5.7%) for the Eq. (2). The last stage reveals a weight loss of 14.5% at 350.9 °C due to the formation of PbO, which is in accordance with the Eq. (3) [18,19]:

$$(PbCO_3)_2 \cdot Pb(OH)_2 \rightarrow (PbCO_3)_2 \cdot PbO + H_2O \quad (1)$$

$$(PbCO_3)_2 \cdot PbO \rightarrow PbCO_3 \cdot (PbO)_2 + CO_2 \quad (2)$$

$$PbCO_3 \cdot (PbO)_2 \rightarrow 3PbO + CO_2 \quad (3)$$

For $CuCO_3 \cdot Cu(OH)_2$, the decomposition process takes place in single step at 305.8 °C according to the Eq. (4) [20]:

$$1/2(CuCO_3 \cdot Cu(OH)_2) \rightarrow CuO + 1/2CO_2 + 1/2H_2O \quad (4)$$

The curves also indicate that this decomposition process is an endothermic reaction with a weight loss of 27.7%, corresponding to the formation of copper oxide.

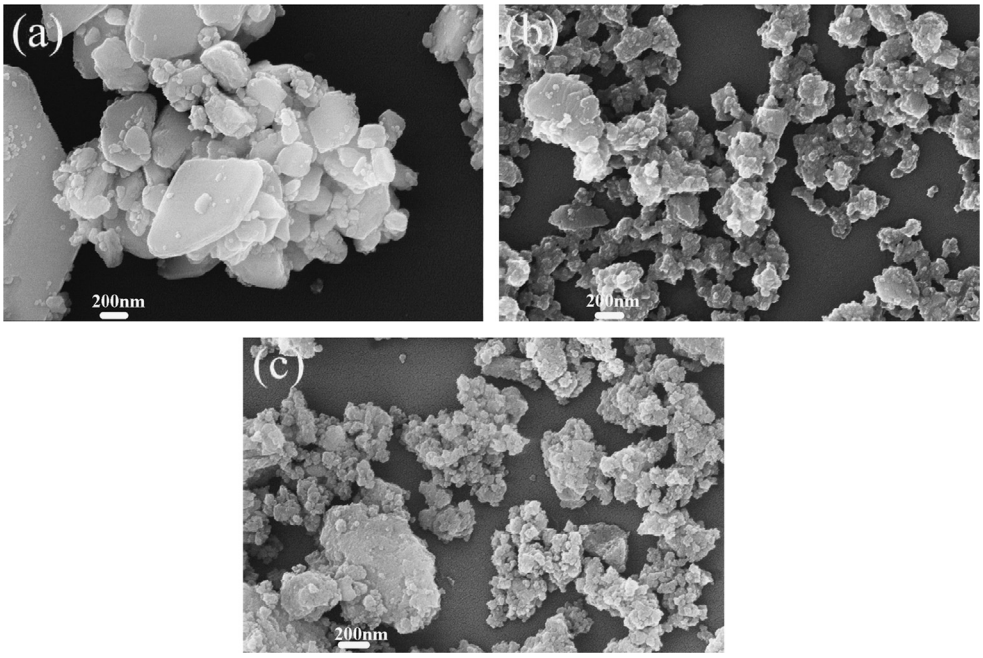

Fig. 2. SEM images of (a) $(PbCO_3)_2 \cdot Pb(OH)_2$, (b) $CuCO_3 \cdot Cu(OH)_2$ and (c) $NiCO_3 \cdot 2Ni(OH)_2 \cdot 4H_2O$.

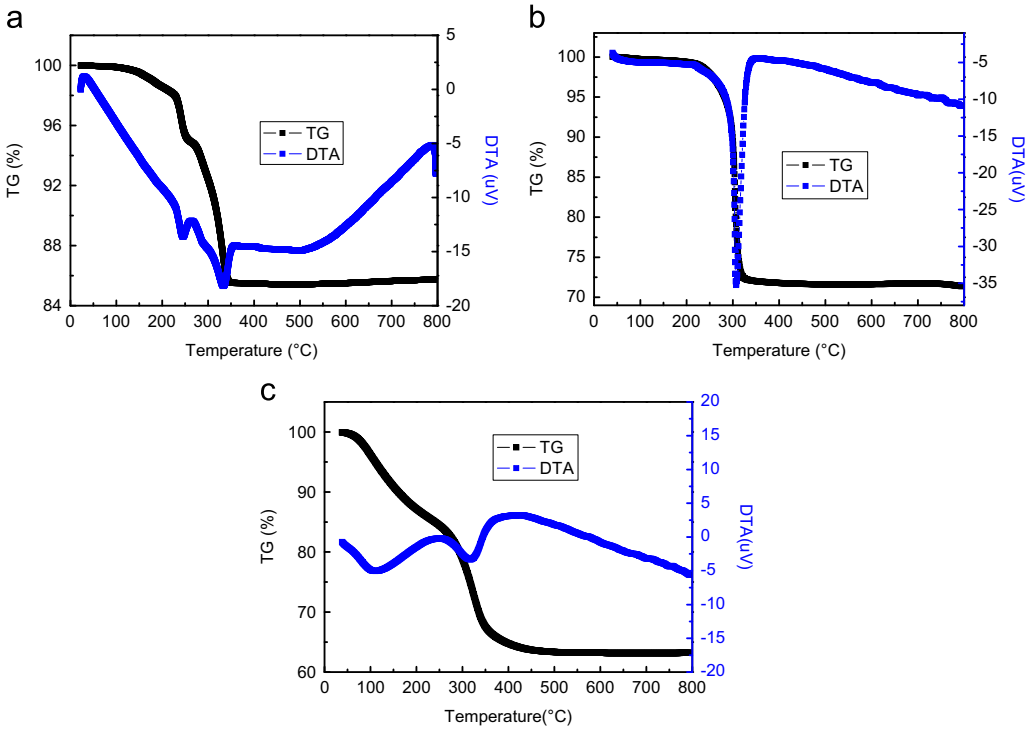

Fig. 3. TG-DTA curves of (a) $(PbCO_3)_2 \cdot Pb(OH)_2$, (b) $CuCO_3 \cdot Cu(OH)_2$ and (c) $NiCO_3 \cdot 2Ni(OH)_2 \cdot 4H_2O$.

Viewed from the TG curve of $NiCO_3 \cdot 2Ni(OH)_2 \cdot 4H_2O$ as shown in Fig. 3c, it is obvious that the decomposition reaction occurs in two steps. The first step ends at 265.1 °C with a residual mass value of 83.5% attributed to the weight loss of 4 mol crystal water per formula. The second process ends at around 441.3 °C with a weight loss of 19.8%, which is associated with the formation of nickel oxide and the evolution of water and carbon dioxide. The DTA curve gives two endothermic peaks at 112.0 and 318.8 °C corresponding to the evolution of water and the formation of nickel oxide. These two decomposition processes can be described by the Eqs. (5) and (6) [21,22].

$$NiCO_3 \cdot 2Ni(OH)_2 \cdot 4H_2O \rightarrow NiCO_3 \cdot 2Ni(OH)_2 + 4H_2O \quad (5)$$

$$NiCO_3 \cdot 2Ni(OH)_2 \rightarrow 3NiO + CO_2 + 2H_2O \quad (6)$$

The electrochemical conversion reactions of basic carbonates are studied by cyclic voltammetry. The first three cyclic voltammogram curves of the three basic carbonates at a scan rate of 0.1 mV s^{-1} are evaluated and compared in Fig. 4a–c to understand the detailed electrochemical process. For $(PbCO_3)_2 \cdot Pb(OH)_2$, there are two reduction peaks appear at 1.66 and 1.42 V, and five oxidation peaks appear at 0.60, 0.68, 1.18, 1.54 and 2.12 V in the initial cycle. The peak at about 1.66 V is probably attributed to the decomposition of $(PbCO_3)_2 \cdot Pb(OH)_2$ and the following electrochemical reaction of $PbCO_3$ ($\Delta_f G_m = -625.5$ KJ mol^{-1}) with Li during the preliminary Li-ion insertion. The obvious peak at 1.42 V is assigned to the further decomposition of $Pb(OH)_2$ ($\Delta_f G_m = -427.7$ KJ mol^{-1}) and the formation of LiOH and Pb. These characteristic behaviors almost disappear in the subsequent cycles, illustrating the irreversibility of these decomposition reactions. In the oxidation portion of CV curves, the first four peaks is attributed to the extraction of Li-ion and the last weak peak at about 2.12 V probably corresponds to the regeneration of trace $PbCO_3$ and Pb $(OH)_2$. After the initial cycle, the following CV curves coincide well with each other, revealing that the conversion reaction becomes reversible in the subsequent cycles. In the following two cycles, the new reduction peak at around 0.43 V that is sheltered in the initial cycle may be related to the formation of different Li_xPb alloys ($1.0 \leq x \leq 4.4$) [23]. While the oxidation peaks at 0.61 and 0.72 V may correspond to the de-alloying process. Therefore, these electrochemical reactions can be mainly summarized as the following reactions:

$$(PbCO_3)_2 \cdot Pb(OH)_2 + 6Li^+ + 6e^- \rightarrow 3Pb + 2Li_2CO_3 + 2LiOH \quad (7)$$

$$\text{Main reaction} \quad Pb + xLi^+ + xe^- \leftrightarrow Li_xPb \quad (8)$$

$$\text{Trace reaction} \quad Pb + Li_2CO_3 \leftrightarrow PbCO_3 + 2Li^+ + 2e^- \quad (9)$$

$$\text{Trace reaction} \quad Pb + 2LiOH \leftrightarrow Pb(OH)_2 + 2Li^+ + 2e^- \quad (10)$$

Compared with the $(PbCO_3)_2 \cdot Pb(OH)_2$, the electrochemical processes of basic nickel carbonate hydrate and basic copper carbonate show similar characteristics with each other. In the first CV curve of $CuCO_3 \cdot Cu(OH)_2$, two reduction peaks appear at 1.59 and 0.37 V, corresponding to the decomposition of $CuCO_3 \cdot Cu(OH)_2$, the following electrochemical reactions of $CuCO_3$ and $Cu(OH)_2$ with Li and the formation of SEI film [24,25]. During the following charge, four weak oxidation peaks at 0.82, 1.15, 1.85 and 2.31 V are probably attributed to the probable oxidation process of Cu to $Cu(OH)_2$

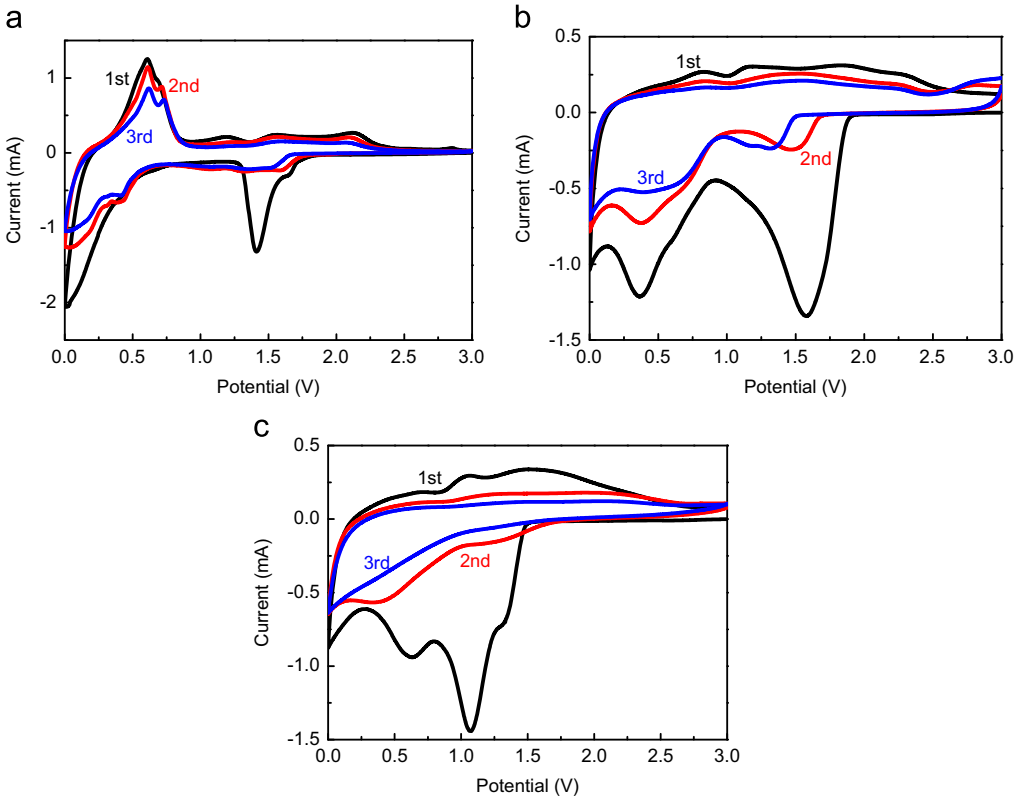

Fig. 4. Cyclic voltammogram curves of (a) $(PbCO_3)_2 \cdot Pb(OH)_2$, (b) $CuCO_3 \cdot Cu(OH)_2$ and (c) $NiCO_3 \cdot 2Ni(OH)_2 \cdot 4H_2O$.

($\Delta_f G_m = -357.7$ KJ mol^{-1}) and $CuCO_3$ ($\Delta_f G_m = -595.5$ KJ mol^{-1}). In the 2nd and 3rd cycles, two reduction peaks at 1.47 and 0.37 V and three oxidation peaks at 0.85, 1.53 and 2.32 V can be observed with the decrease of individual peak intensity and integral area indicating the irreversible capacity loss. The detailed reaction mechanism can be described as the following equations:

$$CuCO_3 \cdot Cu(OH)_2 + 4Li^+ + 4e^- \rightarrow 2Cu + Li_2CO_3 + 2LiOH \quad (11)$$

$$2LiOH + Cu \leftrightarrow Cu(OH)_2 + 2Li^+ + 2e^- \quad (12)$$

$$Li_2CO_3 + Cu \leftrightarrow CuCO_3 + 2Li^+ + 2e^- \quad (13)$$

For $NiCO_3 \cdot 2Ni(OH)_2 \cdot 4H_2O$, there is a small reduction peak at 1.33 V in the first reduction process, which is associated with the preliminary reaction of Li-ion insertion and the decomposition of $NiCO_3 \cdot 2Ni(OH)_2 \cdot 4H_2O$. After that, two strong reduction peaks can be found at 1.07 and 0.63 V, corresponding to the reduction of Ni^{2+} to Ni^0 in $NiCO_3$ ($\Delta_f G_m = -514.2$ KJ mol^{-1}) and $Ni(OH)_2$ ($\Delta_f G_m = -447.3$ KJ mol^{-1}), respectively. In the reverse oxidation process, two oxidation peaks at 1.03 and 1.67 V are observed, corresponding to the extraction of Li from Ni/LiOH and Ni/Li_2CO_3 mixtures with the oxidation of Ni^0 to Ni^{2+} [26], whereas the reduction peaks become weaker and the peak current becomes smaller in the following two cycles, exhibiting a poor electrochemical properties. Hence, the electrochemical reaction of Li with $NiCO_3 \cdot 2Ni(OH)_2 \cdot 4H_2O$ can be probably expressed as the following equations:

$$NiCO_3 \cdot 2Ni(OH)_2 \cdot 4H_2O + 6Li^+ + 6e^- \rightarrow 3Ni + Li_2CO_3 + 4LiOH + 4H_2O \quad (14)$$

$$2LiOH + Ni \leftrightarrow Ni(OH)_2 + 2Li^+ + 2e^- \quad (15)$$

$$Li_2CO_3 + Ni \leftrightarrow NiCO_3 + 2Li^+ + 2e^- \quad (16)$$

Fig. 5a–c shows the charge–discharge curves and corresponding cycling properties of the three basic carbonates. The lithiation and delithiation plateaus in the potential profiles are well consistent with the CV peaks as shown in Fig. 4a–c. The $(PbCO_3)_2 \cdot Pb(OH)_2$ shows a discharge capacity of 1175.8 mAh g^{-1} and a charge capacity of 642.1 mAh g^{-1} in the initial cycle, corresponding to a coulombic efficiency of 54.6%. The large irreversible capacity can be ascribed to the SEI film formation and the partial inactivation of some particles after the initial cycle. However, the theoretical lithium storage capacity of $(PbCO_3)_2 \cdot Pb(OH)_2$ is around 560.2 m Ah g^{-1} based on the Eq. (7). It should be noticed that the initial charge capacity is larger than the theoretical capacity, corresponding to the partial oxidation decomposition of SEI film and the extraction of Li-ion from Pb/Li_2CO_3 and Pb/LiOH grain boundaries [23]. In the following cycles between the 2nd and 20th cycles, the charge specific capacities reduce from 517.6 to 77.2 mAh g^{-1} due to the formation/decomposition of SEI film, particle pulverization and electrode collapse. Fig. 5b illustrates the charge/discharge profiles of $CuCO_3 \cdot Cu(OH)_2$. It is clear that the first discharge capacity is 1356.2 mAh g^{-1} and

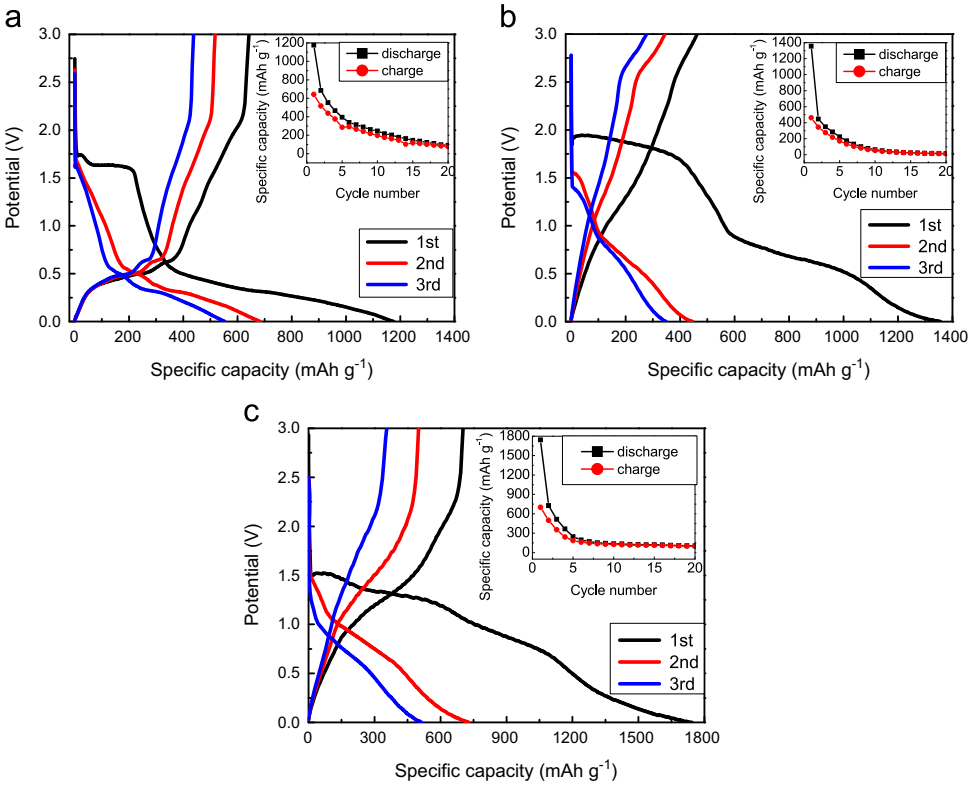

Fig. 5. Charge–discharge curves and corresponding cyclic performances of basic metal carbonates at a current density of 50 mA g^{-1} between 0.0 and 3.0 V. (a) $(PbCO_3)_2 \cdot Pb(OH)_2$; (b) $CuCO_3 \cdot Cu(OH)_2$; (c) $NiCO_3 \cdot 2Ni(OH)_2 \cdot 4H_2O$.

the charge capacity is 462.7 mAh g^{-1}. The first discharge capacity exceeds the theoretical value (485.0 mAh g^{-1}), which is calculated according to the Eq. (11). The extra capacity can be attributed to the formation of SEI film during the first discharge process and the probable lithium storage on interface [27–30]. The cyclic performance curve of $CuCO_3 \cdot Cu(OH)_2$ exhibits a decrease in the discharge capacity from 1356.2 to 14.6 mAh g^{-1} after 20 cycles, indicating a poor cyclic performance. The reason can be assigned to that Li_2CO_3 and LiOH arising from the reduction of $CuCO_3 \cdot Cu(OH)_2$ cannot be reduced to Li completely in the charge process, and the continuous particle pulverization per cycle leads to the capacity fading in the following charge–discharge cycling. Being similar to $(PbCO_3)_2 \cdot Pb(OH)_2$ and $CuCO_3 \cdot Cu(OH)_2$, $NiCO_3 \cdot 2Ni(OH)_2 \cdot 4H_2O$ delivers a discharge capacity of 1742.6 mAh g^{-1} in the first cycle, which is much higher than the theoretical value (427.7 mAh g^{-1}). The extra capacity should correspond to the growth of SEI film on the surface of the active particles and the probable lithium storage on interface in the initial discharge process [29,30]. After 20 cycles, the discharge and charge capacities are maintained at 104.3 and 98.1 mAh g^{-1}, respectively. The reason of poor cyclic performance of $NiCO_3 \cdot 2Ni(OH)_2 \cdot 4H_2O$ is similar to $CuCO_3 \cdot Cu(OH)_2$. In addition, the capacity retention of $NiCO_3 \cdot 2Ni(OH)_2 \cdot 4H_2O$ (14.0%) after 20 cycles is higher than the other two basic metal carbonates ($(PbCO_3)_2 \cdot Pb(OH)_2$: 12.0%; $CuCO_3 \cdot Cu(OH)_2$: 2.9%) due to its smaller

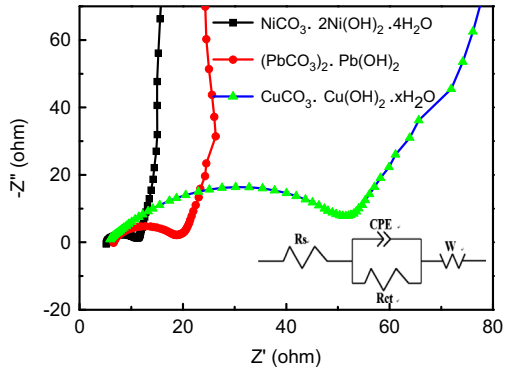

Fig. 6. Nyquist plots of basic metal carbonate electrodes obtained by applying an amplitude of 5.0 mV over the frequency range from 100 kHz to 0.01 Hz.

particle size. Therefore, capacity retention can be increased by reducing the particle size of active particles.

In order to understand different electrochemical performances among the three basic carbonates, the electrochemical impedance spectra obtained in the frequency range from 100 kHz to 0.01 Hz before the initial cycle are shown in Fig. 6. All the three electrochemical impedance spectra consist of one semicircle in the high/medium frequency region and a line in the low frequency region. The medium-frequency semicircle can correspond to the charge-transfer process (R_{ct}), while the sloping line in the low frequency region can be ascribed to the lithium-ion diffusion process (Warburg

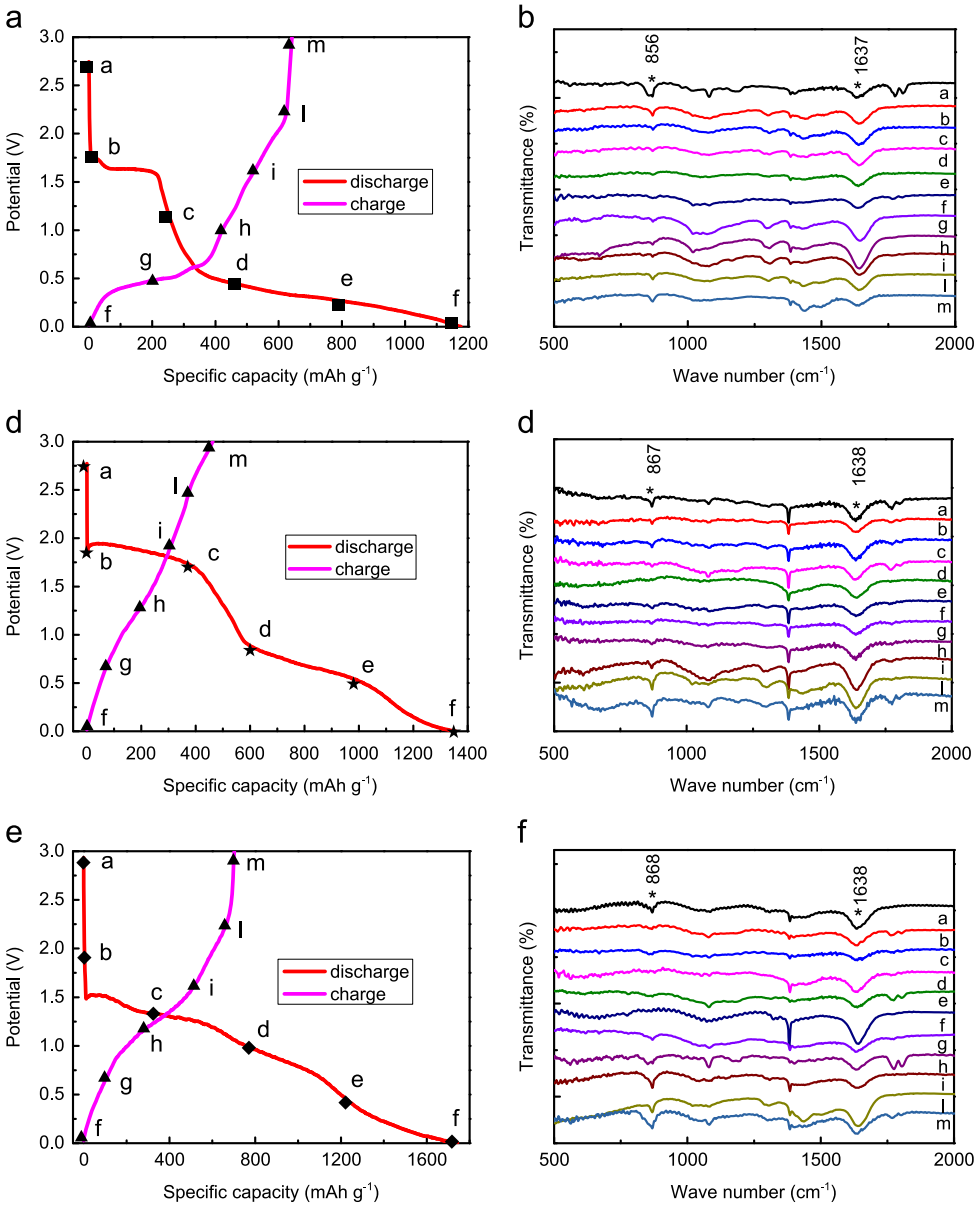

Fig. 7. *Ex-situ* IR spectra of lithiated and delithiated samples during the initial charge–discharge process. (a, b) $(PbCO_3)_2 \cdot Pb(OH)_2$, (c, d) $CuCO_3 \cdot Cu(OH)_2$, (e, f) $NiCO_3 \cdot 2Ni(OH)_2 \cdot 4H_2O$.

impedance, *W*). A simplified equivalent circuit inserted in Fig. 6 is used to fit the impedance spectra, which includes the electrolyte and battery component resistance (R_s), a constant phase element (CPE) corresponded to the interfacial resistance, R_{ct} and *W*. It is obvious that the R_{ct} of $NiCO_3 \cdot 2Ni(OH)_2 \cdot 4H_2O$ is much smaller than those of the other two basic carbonates, indicating that the kinetic properties of $NiCO_3 \cdot 2Ni(OH)_2 \cdot 4H_2O$ are better than those of the other two basic carbonates. And the kinetic properties of $(PbCO_3)_2 \cdot Pb(OH)_2$ are also better than those of $CuCO_3 \cdot Cu(OH)_2$. These results are in accordance with the results of the electrochemical performance as shown in Fig. 5.

In recent years, many investigations have been made on the lithium storage mechanism of transition metal oxides. However, only Zhou and our group [13-15,17] have reported the electrochemical conversion mechanism for lithium storage in manganese and cobalt carbonates. In order to understand the lithium storage mechanisms in basic carbonates, we utilize *ex-situ* FTIR, *ex-situ* XRD and *in-situ* XRD techniques to make a careful study of the structural evolutions of basic carbonates in the initial charge–discharge cycle. We assembled eleven simulated batteries in the *ex-situ* FTIR and *ex-situ* XRD experiments. Among these eleven batteries, we prepared six lithiated samples with the names of (a–f) as shown in Fig. 7a, c and e. In the reverse charge process, five delithiated samples are named as (g), (h), (i), (l) and (m).

Fig. 7b, d and f shows the *ex-situ* IR spectra of the three basic carbonates. The characteristic bands at 1637 and 1368 cm^{-1} can be assigned to the bending vibrations of O–H group, which shows a reversible decrease/increase

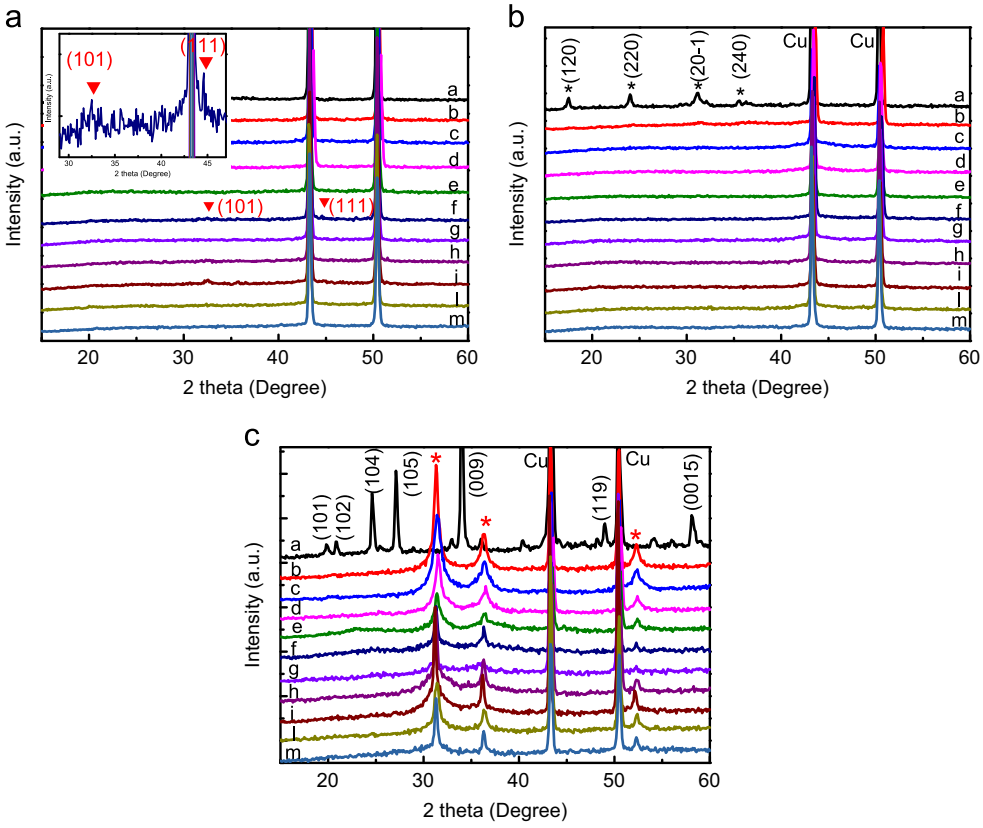

Fig. 8. *Ex-situ* XRD patterns of lithiated and delithiated samples during the initial charge–discharge process. (a) $NiCO_3 \cdot 2Ni(OH)_2 \cdot 4H_2O$; (b) $CuCO_3 \cdot Cu(OH)_2$; (c) $(PbCO_3)_2 \cdot Pb(OH)_2$.

behavior upon lithiation/delithiation process for $(PbCO_3)_2 \cdot Pb(OH)_2$ and $CuCO_3 \cdot Cu(OH)_2$. For comparison, no obvious trend can be observed for $NiCO_3 \cdot 2Ni(OH)_2 \cdot 4H_2O$ due to the existence of crystal water. The adsorption bands at around 856, 867 and 868 cm^{-1}, which can be associated with the CO_3^{2-} in $(PbCO_3)_2 \cdot Pb(OH)_2$ [31,32], $CuCO_3 \cdot Cu(OH)_2$ [33] and NiC $O_3 \cdot 2Ni(OH)_2 \cdot 4H_2O$ [34] respectively, decrease gradually from pattern (a) to pattern (f) in the spectra. This phenomenon indicates that a probable transformation reaction of basic metal carbonate to Li_2CO_3 in the discharge process. In addition, the relative intensity of these characteristic bands increase in the spectra from pattern (f) to pattern (m), corresponding to a partial reverse transformation process of Li_2CO_3 to basic carbonate.

To gain a better understanding of the lithium storage mechanisms in basic metal carbonates, we use the *ex-situ* XRD technique on the three basic carbonates electrodes at selected charge/discharge capacities. As shown in Fig. 8a, the diffraction peaks of $NiCO_3 \cdot 2Ni(OH)_2 \cdot 4H_2O$ become weaker and finally disappear during the discharge process. Simultaneously, two weak peaks located at 32.6° and 44.5° are observed in the inserted figure, which are associated with the (101) peak of LiOH (JCPDS card no. 85-1064) and the (111) peak of Ni (JCPDS card no. 87-0712), respectively, indicating that the transformation process of Ni^{2+} to Ni^0 as shown in Eq. (14). However, the new peaks disappear and no characteristic peaks of $NiCO_3 \cdot 2Ni(OH)_2 \cdot 4H_2O$ can be detected in the whole charge process, indicating the formation of amorphous phase due to the electrochemical reaction. For $CuCO_3 \cdot Cu(OH)_2$ as shown in Fig. 8b, the characteristic (120), (220), (20−1) and (240) peaks of the initial $CuCO_3 \cdot Cu(OH)_2$ electrode at 17.6°, 24.1°, 31.2° and 35.5°, respectively, totally disappear after lithium ion insertion. However, no featured peak attributed to LiOH, Li_2CO_3, and Cu can be observed at the end of discharge. In the charge process, the characteristic peaks of $CuCO_3 \cdot Cu(OH)_2$ do not re-appear and the initial material cannot return to its original phase. As reported, this phenomenon also exists in the electrochemical cycles of metal hydroxide, cobalt chloride and cobalt carbonate [14,35,36]. It demonstrates that the initial discharge process leads to the pulverization of active particles and the amorphization of structure due to the formation of nano-sized metal M, LiOH and Li_2CO_3, and then the pristine structure of basic metal carbonates cannot be restored reversibly in the charge process. In addition, the *ex-situ* XRD results also show that the poor cycling behaviors of basic metal carbonates might be due to the particle pulverization, structural collapse and amorphization process of the materials.

For comparison, the lithium storage mechanisms in $(PbCO_3)_2 \cdot Pb(OH)_2$ is more complex than the other two basic carbonates due to the alloying reaction between Li and Pb. In order to better understand the lithium storage mechanism,

we made a thorough investigation about the structural evolutions of $(PbCO_3)_2 \cdot Pb(OH)_2$ combined by using *ex-situ* and *in-situ* XRD techniques.

As shown in Fig. 8c, all the peaks corresponding to $(PbCO_3)_2 \cdot Pb(OH)_2$ disappear during the discharge process indicating complete structural decomposition. An interesting observation is the appearance of diffraction peaks at 31.3°, 36.3° and 52.3°, ascribed to the formation of metal Pb at the begin of the discharge process. Viewed from pattern (b) to pattern (d), the two Bragg positions (31.3° and 36.3°) gradually shift to higher angles owing to the phase transformation from Pb to LiPb (JCPDS card no.10-0233). Then the Bragg positions shift to lower angles from curve (d) to curve (f) due to the formation of Li_8Pb_3 from LiPb. In the charge process, the reverse shifting of Bragg positions suggests the phase transformation from Li_8Pb_3 to LiPb and then to Pb.

Based on the *ex-situ* XRD results, we preliminarily understand the lithium storage mechanism of $(PbCO_3)_2 \cdot Pb(OH)_2$. However, the information of the alloying reaction is not comprehensive. In order to further investigate the structural evolution during the charge–discharge cycle, we observe the structural evolutions of $(PbCO_3)_2 \cdot Pb(OH)_2$ by using *in-situ* XRD technique.

The structure and equipment of the *in-situ* XRD battery were described in our previous paper [37]. As shown in Fig. 9a, the diffraction peaks at 38.4°, 41.2° and 43.9° are attributed to beryllium oxide, according to the JCPDS card no.78-1553 and previous reports [38,39]. The featured diffraction peaks of $(PbCO_3)_2 \cdot Pb(OH)_2$ located at 24.7°, 27.3°, 34.1°, 40.4°, 43.0°, and 42.6° disappear along with the lithiation process. However, most peaks cannot reappear and only a weak peak at 24.7° emerges during delithiation, indicating that the charge/discharge process is a partially reversible reaction. Besides, a new weak diffraction peak at 31.3° appears and shows a slight increase upon the discharge process, corresponding to the formation of Pb (JCPDS card no. 04-0686) and Li_xPb alloys as shown in Fig. 9a and b. In the reverse charge process, the increase of the diffraction peaks at 31.3° and 36.2° can be attributed to the transformation from Li_8Pb_3 to Pb. Moreover, the aggregation of Pb particles results in the sharp diffraction peaks at 31.3° and 36.2°.

In addition, we performed the *ex-situ* SAED and HRTEM observation to confirm the final products of the lithiated $(PbCO_3)_2 \cdot Pb(OH)_2$ electrode. The electrode was prepared by mixing $(PbCO_3)_2 \cdot Pb(OH)_2$ and carbon black at a weight ratio of 9:1 and then discharged to 0 V at 50 mA g^{-1}. Fig. 10a

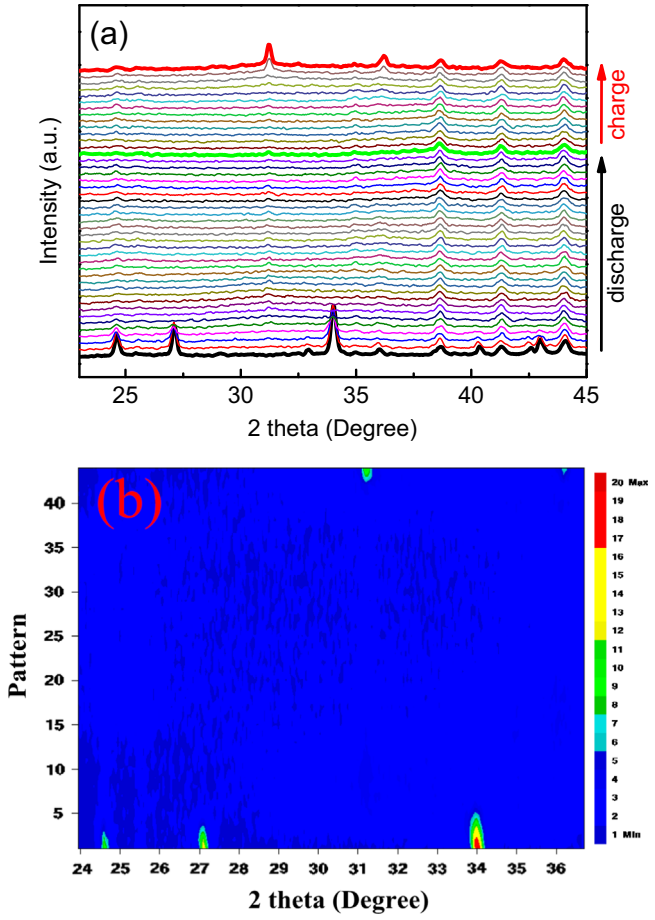

Fig. 9. (a) *In-situ* XRD patterns of $(PbCO_3)_2 \cdot Pb(OH)_2$ cycled between 0.0 and 3.0 V at a current density of 50 mA g^{-1}; (b) a close-up shot of diffraction peaks *vs.* intensity in the angle range 24–44°.

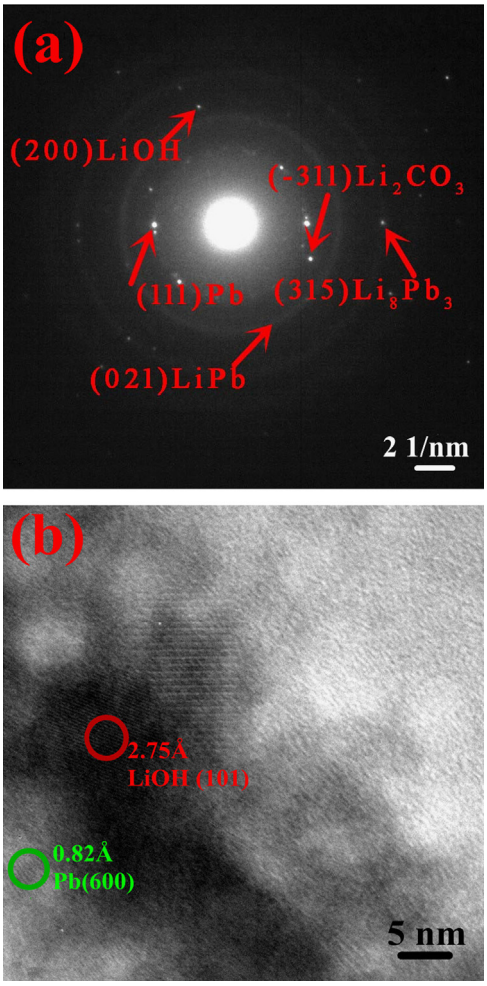

Fig. 10. *Ex-situ* SAED (a) and HRTEM (b) images of lithiated $(PbCO_3)_2 \cdot Pb(OH)_2$ after a discharge to 0.0 V.

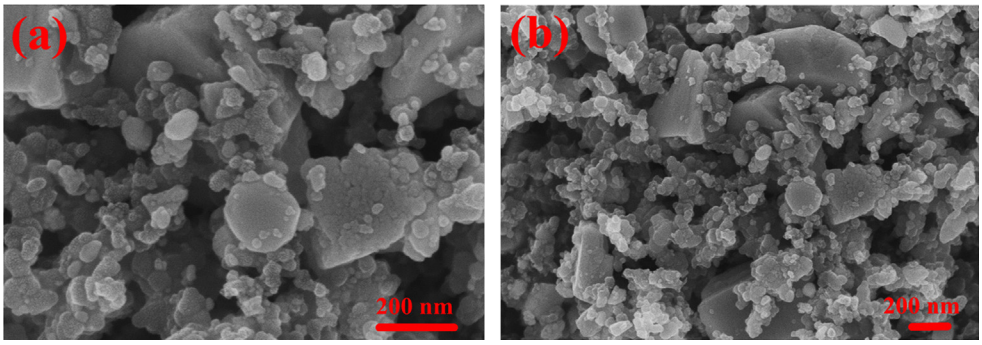

Fig. 11. SEM images of carbon black-$(PbCO_3)_2 \cdot Pb(OH)_2$ composite (a, b) after ball-milling.

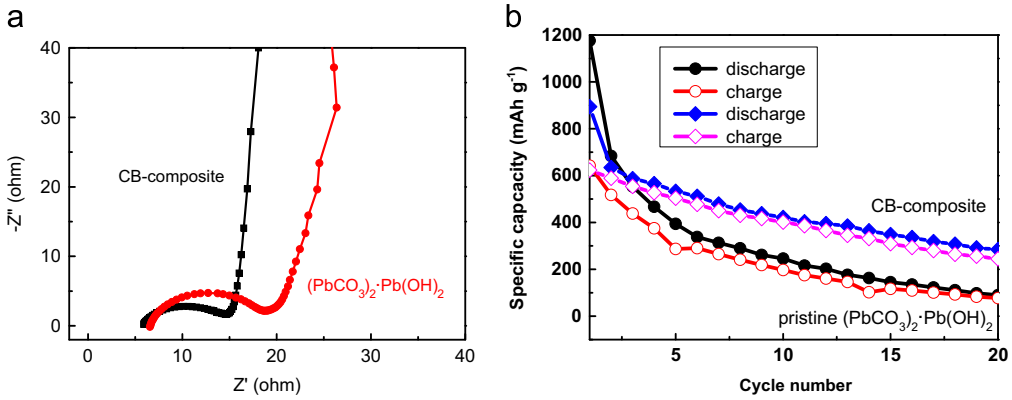

Fig. 12. EIS spectra (a) and cycling properties (b) of pristine $(PbCO_3)_2 \cdot Pb(OH)_2$ and its carbon black composite.

shows the SAED pattern for lithiated $(PbCO_3)_2 \cdot Pb(OH)_2$. It is clear that the observed well-defined rings can be confirmed as Pb (111), Li_2CO_3 (−311), LiPb (021), LiOH (200) and Li_8Pb_3 (315), indicating the formed polycrystalline phases as shown in Eq. (7). Besides, HRTEM image (Fig. 10b) shows that a large amount of nanocrystallines are dispersed in a disordered matrix. The characteristic lattice distances of partial final products are measured to be 0.82 and 2.75 Å, which are in accordance with the (600) plane of unreacted Pb and the (101) of LiOH, respectively. According to the above results and previous reports on the reversible reactions of metal oxides [40,41], the lithium storage mechanisms in $(PbCO_3)_2 \cdot Pb(OH)_2$ are well consistent with the proposed reaction mechanisms as shown in the Eqs. (7)–(10), and the lithiation/delithiation process is a partially reversible.

In the experiment, the electrochemical properties of as-obtained samples are poor due to the possible particle pulverization and structural breakdown. Here, $(PbCO_3)_2 \cdot Pb(OH)_2$ was mixed with carbon black in a weight ratio of 3:1 by a high-energy ball milling for 20 h to improve the cycling stability. As the SEM images shown in Fig. 11, the $(PbCO_3)_2 \cdot Pb(OH)_2$ was well-dispersed in the carbon black matrix after ball-milling. As a result, the electronic conductivity and charge transfer speed (Fig. 12a) of $(PbCO_3)_2 \cdot Pb(OH)_2$ are greatly improved by introducing carbon black and smaller particle size. As shown in Fig. 12b, carbon black–$(PbCO_3)_2 \cdot Pb(OH)_2$ composite shows better electrochemical properties than that of the pristine sample. It can deliver a reversible charge capacity of 244.7 mAh g^{-1} after 20 cycles, which is much higher than the value (77.2 mAh g^{-1}) of the pristine sample. The improved electrochemical performance should be attributed to the smaller particle size and the introduced carbon black as conductive additive and buffer layer.

4. Conclusions

In this paper, three basic metal carbonates ($(PbCO_3)_2 \cdot Pb(OH)_2$, $NiCO_3 \cdot 2Ni(OH)_2 \cdot 4H_2O$ and $CuCO_3 \cdot Cu(OH)_2$) are investigated for the first time as probable anode materials for lithium-ion batteries. All the three basic carbonates can deliver high initial discharge and charge specific capacities, which are much higher than their theoretical values. The high initial reversible charge capacity can be attributed to the extraction of Li-ion from Li_xM alloys, M/Li_2CO_3 and M/LiOH (M = Pb, Ni, Cu) mixtures and their grain boundaries. In addition, the capacity retention of $NiCO_3 \cdot 2Ni(OH)_2 \cdot 4H_2O$ (14.0%) after 20 cycles is higher than the other two basic metal carbonates ($(PbCO_3)_2 \cdot Pb(OH)_2$: 12.0%; $CuCO_3 \cdot Cu(OH)_2$: 2.9%) due to its smaller particle size. Therefore, capacity retention and reversible capacity can be increased by reducing the particle size. The electrochemical reaction mechanisms of basic carbonates ($MCO_3 \cdot yM(OH)_2 \cdot zH_2O$) with Li were studied by e*x-situ* FTIR, *ex-situ* XRD, *ex-situ* SAED, *ex-situ* HRTEM

and *in-situ* XRD techniques. For $CuCO_3 \cdot Cu(OH)_2$ and $NiCO_3 \cdot 2Ni(OH)_2 \cdot 4H_2O$, the initial discharge process leads to the formation of metal Cu (or Ni), Li_2CO_3, LiOH and crystal water. For comparison, the initial electrochemical reactions of $(PbCO_3)_2 \cdot Pb(OH)_2$ with Li not only result in the formation of Pb, LiOH, Li_2CO_3 but also show the Li-alloying reaction of Pb. Upon the charge process, the de-alloying reaction and the formation of some MCO_3 and $M(OH)_2$ particles should be responsible for the reversible lithium storage capacity. However, the irreversible capacity is large due to the electrochemical inactivity of active particles after repeated cycles. To suppress the particle pulverization and structural collapse, carbon black was introduced to improve the electrochemical properties of $(PbCO_3)_2 \cdot Pb(OH)_2$. Besides, the particles size of $(PbCO_3)_2 \cdot Pb(OH)_2$ was also crushed by high-energy ball-milling. It is obvious that carbon black-$(PbCO_3)_2 \cdot Pb(OH)_2$ composite can deliver a high reversible charge specific capacity of 244.7 mAh g^{-1} with capacity retention of 39.2% after 20 cycles. Therefore, basic metal carbonates can be developed as potential lithium storage materials for high capacity batteries.

Acknowledgments

This work is sponsored by the National 863 Program (2013AA050901) and the National Natural Science Foundation of China (No. 51104092). The work is also supported by K.C. Wong Magna Fund in Ningbo University, Open Foundation of State Key Laboratory of Materials Processing and Die & Mould Technology (2012-P01), Open Foundation of State Key Laboratory of Electronic Thin Films and Integrated Devices (KFJJ201209) and Opening Project of State Key Laboratory of High Performance Ceramics and Superfine Microstructure (SKL201308SIC).

References

[1] Y.P. Wu, C. Jiang, C. Wan, R. Holze, Modified natural graphite as anode material for lithium ion batteries, Journal of Power Sources 111 (2002) 329–334.

[2] W.A. Ang, N. Gupta, R. Prasanth, S. Madhavi, High-performing mesoporous iron oxalate anodes for lithium-ion batteries, ACS Applied Materials & Interfaces 4 (2012) 7011–7019.

[3] L.F. Shen, H.S. Li, E. Uchaker, X.G. Zhang, G.Z. Cao, General strategy for designing core-shell nanostructured materials for high-power lithium ion batteries, Nano Letters 12 (2012) 5673–5678.

[4] L.B. Chen, N. Lu, C.M. Xu, H.C. Yu, T.H. Wang, Electrochemical performance of polycrystalline CuO nanowires as anode material for Li ion batteries, Electrochimica Acta 54 (2009) 4198–4201.

[5] G.H. Zhang, Y.J. Chen, B.H. Qu, L.L. Hu, L. Mei, D.N. Lei, Q. Li, L.B. Chen, Q.H. Li, T.H. Wang, Synthesis of mesoporous NiO nanospheres as anode materials for lithium ion batteries, Electrochimica Acta 80 (2012) 140–147.

[6] M.W. Xu, F. Wang, M.S. Zhao, S. Yang, X.P. Song, Molten hydroxides synthesis of hierarchical cobalt oxide nanostructure and its application as anode material for lithium ion batteries, Electrochimica Acta 56 (2011) 4876–4881.

[7] B. Sun, Z.X. Chen, H.S. Kim, H. Ahn, G.X. Wang, MnO/C core–shell nanorods as high capacity anode materials for lithium-ion batteries, Journal of Power Sources 196 (2011) 3346–3349.

[8] Y.X. Chen, L.H. He, P.J. Shang, Q.L. Tang, Z.Q. Liu, H.B. Liu, L.P. Zhou, Micro-sized and nano-sized Fe_3O_4 particles as anode materials for lithium-ion batteries, Journal of Materials Science & Technology 27 (2011) 41–45.

[9] A.K. Rai, L.T. Anh, J. Gim, J. Kim, One-step synthesis of CoO anode material for rechargeable lithium-ion batteries, Ceramics International 39 (2013) 9325–9330.

[10] S.M. Abbas, S.T. Hussain, S. Ali, F. Abbas, N. Ahmad, N. Ali, Y. Khan, One-pot synthesis of a composite of monodispersed CuO nanospheres on carbon nanotubes as anode material for lithium-ion batteries, Journal of Alloys and Compounds 574 (2013) 221–226.

[11] S.D. Seo, D.H. Lee, J.C. Kim, G.H. Lee, D.W. Kim, Room-temperature synthesis of CuO/graphene nanocomposite electrodes for high lithium storage capacity, Ceramics International 39 (2013) 1749–1755.

[12] B. Wang, J.L. Cheng, Y.P. Wu, D. Wang, D.N. He, Porous NiO fibers prepared by electrospinning as high performance anode materials for lithium ion batteries, Electrochemistry Communications 23 (2012) 5–8.

[13] L.Y. Shao, J. Shu, R. Ma, M. Shui, L. Hou, K.Q. Wu, D.J. Wang, Y.L. Ren, Electrochemical characteristics and intercalation mechanism of manganese carbonate as anode material for lithium-ion batteries, International Journal of Electrochemical Science 8 (2013) 1170–1180.

[14] L.W. Su, Z. Zhou, X. Qin, Q.W. Tang, D.H. Wu, P.W. Shen, $CoCO_3$ submicrocube/grapheme composites with high lithium storage capability, Nano Energy 2 (2013) 276–282.

[15] L.Y. Shao, R. Ma, K.Q. Wu, M. Shui, M.M. Lao, D.J. Wang, N.B. Long, Y.L. Ren, J. Shu, Metal carbonates as anode materials for lithium ion batteries, Journal of Alloys and Compounds 581 (2013) 602–609.

[16] S. Mirhashemihaghighi, B. Leon, C.P. Vicente, J.L. Tirado, R. Stoyanova, M. Yoncheva, E. Zhecheva, R.S. Puche, E.M. Arroyo, J.R. Paz, Lithium storage mechanisms and effect of partial cobalt substitution in manganese carbonate electrodes, Inorganic Chemistry 51 (2012) 5554–5560.

[17] L.Y. Shao, S.Y. Wang, K.Q. Wu, M. Shui, R. Ma, D.J. Wang, N.B. Long, Y.L. Ren, J. Shu, Comparison of $(BiO)_2CO_3$ to $CdCO_3$ as anode materials for lithium-ion batteries, Ceramics International (2013) http://dx.doi.org/10.1016/j.ceramint.2013.08.140.

[18] B. Drtinova, M. Pospisil, V. Cuba, Products of radiation removal of lead from aqueous solutions, Applied Radiation and Isotopes 68 (2010) 672–675.

[19] G. Chen, E.G. Fu, M. Zhou, Y. Xu, L. Fei, S.G. Deng, V. Chaitanya, Y.Q. Wang, H.M. Luo, A facile microwave-assisted route to $Co(OH)_2$ and Co_3O_4 nanosheet for Li-ion battery, Journal of Alloys and Compounds 578 (2013) 349–354.

[20] W.M. Shaheen, M.M. Selim, Effect of thermal treatment on physico-chemical properties of pure and mixed manganese carbonate and basic copper carbonate, Thermochimica Acta 322 (1998) 117–128.

[21] V. Berbenni, C. Milanese, G. Bruni, A. Marini, The combined effect of mechanical and thermal energy on the solid-state formation of $NiFe_2O_4$ from the system $2NiCO_3 \cdot 3Ni(OH)_2 \cdot 4H_2O$–$FeC_2O_4 \cdot 2H_2O$, Thermochimica Acta 469 (2008) 86–90.

[22] D. Chen, H.Y. Liu, One-step synthesis of nickel ferrite nanoparticles by ultrasonic wave-assisted ball milling technology, Materials Letters 72 (2012) 95–97.

[23] Q.M. Pan, Z.J. Wang, J. Liu, G.P. Yin, M. Gu, PbO@C core–shell nanocomposites as an anode material of lithium-ion batteries, Electrochemistry Communications 11 (2009) 917–920.

[24] S.Q. Wang, J.Y. Zhang, C.H. Chen, Dandelion-like hollow microspheres of CuO as anode material for lithium-ion batteries, Scripta Materialia 57 (2007) 337–340.

[25] C. Liang, M.X. Gao, H.G. Pan, Y.F. Liu, M. Yan, Lithium alloys and metal oxides as high-capacity anode materials for lithium-ion batteries, Journal of Alloys and Compounds 575 (2013) 246–256.

[26] X.F. Li, A. Dhanabalan, C.L. Wang, Enhanced electrochemical performance of porous NiO–Ni nanocomposite anode for lithium ion batteries, Journal of Power Sources 196 (2011) 9625–9630.

[27] Y.J. Mai, X.L. Wang, J.Y. Xiang, Y.Q. Qiao, D. Zhang, C.D. Gu, J.P. Tu, CuO/graphene composite as anode materials for lithium-ion batteries, Electrochimica Acta 56 (2011) 2306–2311.

[28] X.H. Huang, C.B. Wang, S.Y. Zhang, F. Zhou, CuO/C microspheres as anode materials for lithium ion batteries, Electrochimica Acta 56 (2011) 6752–6756.
[29] X.H. Huang, Y.F. Yuan, Z. Wang, S.Y. Zhang, F. Zhou, Electrochemical properties of NiO/Co–P nanocomposite as anode materials for lithium ion batteries, Journal of Alloys and Compounds 509 (2011) 3425–3429.
[30] V. Aravindan, P.S. Kumar, J. Sundaramurthy, W.C. Ling, S. Ramakrishna, S. Madhavi, Electrospun NiO nanofibers as high performance anode material for Li-ion Batteries, Journal of Power Sources 227 (2013) 284–290.
[31] B. Han, W.B. Zhao, X.Y. Qin, Yanhong Li, Y.L. Sun, W. Wei, Synthesis of dimethyl hexane-1,6-diyldicarbamate from 1,6-hexamethylenediamine and methyl carbamate using lead dioxide as catalyst, Catalysis Communications 33 (2013) 38–41.
[32] M.S. Refat, S.M. Teleb, S.A. Sadeek, A novel method for preparation of cobalt (II) and lead (II) carbonates, Spectrochimica Acta Part A: Molecular Spectroscopy 60 (2004) 2803–2805.
[33] T.X. Wang, S.H. Xu, F.X. Yang, Green synthesis of CuO nanoflakes from $CuCO_3 \cdot Cu(OH)_2$ powder and H_2O_2 aqueous solution, Powder Technology 228 (2012) 128–130.
[34] L.Y. Wang, G.Q. Wu, D.G. Evans, Synthesis and characterization of a layered double hydroxide containing an intercalated nickel (II) citrate complex, Materials Chemistry and Physics 104 (2007) 133–140.
[35] S.B. Ni, X.H. Lv, T. Li, X.L. Yang, L.L. Zhang, The investigation of Ni $(OH)_2$/Ni as anode for high performance Li-ion battery, Journal of Materials Chemistry A1 (2013) 1535–1544.
[36] J.L. Liu, W.J. Cui, C.X. Wang, Y.Y. Xia, Electrochemical reaction of lithium with $CoCl_2$ in nonaqueous electrolyte, Electrochemistry Communications 13 (2011) 269–271.
[37] J. Shu, M. Shui, D. Xu, Y.L. Ren, D.J. Wang, Q.C. Wang, R. Ma, W.D. Zheng, S. Gao, L. Hou, J.J. Xu, J. Cui, Z.H. Zhu, Large-scale synthesis of $Li_{1.15}V_3O_8$ nanobelts and their lithium storage behaviors studied by *in-situ* X-ray diffraction, Journal of Materials Chemistry 22 (2012) 3035–3043.
[38] D.D. Thorat, B.M. Tripathi, D. Sathiyamoorthy, Extraction of beryllium from Indian beryl by ammonium hydrofluoride, Hydrometallurgy 109 (2011) 18–22.
[39] J.H. Yum, T. Akyol, M. Lei, D.A. Ferrer, T.W. Hudnall, M. Downer, C.W. Bielawski, G. Bersuker, J.C. Lee, S.K. Banerjee, A study of highly crystalline novel beryllium oxide film using atomic layer deposition, Journal of Crystal Growth 334 (2011) 126–133.
[40] A.K. Jibin, M.V. Reddy, G.V. Subba Rao, U.V. Varadarajua, B.V.R. Chowdari, Pb_3O_4 type antimony oxides MSb_2O_4 (M=Co, Ni) as anode for Li-ion batteries, Electrochimica Acta 71 (2012) 227–232.
[41] J. Shu, R. Ma, L.Y. Shao, M. Shui, D.J. Wang, K.Q. Wu, N.B. Long, Y.L. Ren, Hydrothermal fabrication of lead hydroxide chloride as a novel anode material for lithium-ion batteries, Electrochimica Acta 102 (2013) 381–387.